Experimental observations on Weissenberg number-controlled developing turbulent boundary layers

Zeeshan Saeed
Department of Mechanical Engineering, University of New Hampshire, Durham, New Hampshire 03824, USA

Yasaman Farsiani
Samueli School of Engineering, University of California, Irvine, California 92697, USA

Brian R. Elbing*
Mechanical and Aerospace Engineering, Oklahoma State University, Stillwater, Oklahoma 74078, USA

(Received 15 August 2023; accepted 13 September 2024; published 18 October 2024)

A developing turbulent boundary layer (TBL) was created using a uniform concentration of drag-reducing polymer for which the mean molecular weight was controlled and monitored throughout testing. This obtained a polymer-modified TBL with known polymer properties, including the Weissenberg number (Wi). The resulting mean and fluctuating velocity profiles were measured using particle image velocimetry. Polymeric tests were performed at friction Reynolds numbers (δ^+) ranging from 470 to 760, drag reduction (DR) levels ranging from 0% to 44%, and Wi ranging from 0.2 to 13. In addition to the baseline Newtonian conditions, polymeric conditions were selected such that two had nearly the same Wi with significantly different DR, and two others had the same DR with significantly different Wi. The mean and fluctuating velocity profiles showed Wi dependence, with the suppression of wall-normal velocity fluctuations strongly dependent on Wi. While the streamwise velocity fluctuations (nonscaled) increased only marginally, the significant suppression in the wall-normal velocity fluctuations also indicates that this increase in anisotropic fluctuating velocity field has a Wi dependence. Conditional averaging of the profiles was performed to isolate the impact of Wi on ejection and sweep events: the latter events showed suppression throughout the TBL in proportion to the Wi, while the former events showed similar behavior, but not as uniformly throughout the TBL. Finally, proper orthogonal decomposition was performed to quantify the reduction of complexity within the polymer-modified TBL, for which the reduction was strongly correlated with Wi, even more so than the level of DR. This indicates that the polymer chains effectively subdue specific scales (i.e., smaller scales) so that there is no longer a mere passing of energy through those scales.

DOI: 10.1103/PhysRevFluids.9.104606

I. INTRODUCTION

The use of water-soluble polymers for drag reduction (DR) has a long history of commercial applications [1] and fundamental studies [2–6]. Polymer drag reduction (PDR), in a given turbulent flow, depends on the polymer type, solvent, molecular weight, and concentration. For a developing turbulent boundary layer (TBL), the polymer additives are typically injected upstream, which creates streamwise and wall-normal gradients in polymer concentration [7–13]. In addition, polymer

*Contact author: elbing@okstate.edu

degradation due to flow shear-induced scission of polymer chains causes significant changes to its mean molecular weight (M_w) [14]. Historically, such changes have not been of great concern when studying the polymer-modified mean velocity profiles due to the widely held assumption that the DR was sufficient to characterize the deviation from the Newtonian flows.

Given this assumption, the classical view of polymer-modified mean streamwise velocity profiles had two key elements to it: (i) below maximum drag reduction (MDR), the log region of the TBL was unmodified relative to the classical law-of-the-wall for Newtonian fluids, though shifted outward in proportion to the DR level [3], and (ii) once MDR is achieved, the entire profile beyond the viscous sublayer takes the form of the empirically derived ultimate profile [15]. It is now common to further divide PDR below MDR into the low drag reduction (LDR) and high drag reduction (HDR) regimes. The division between LDR and HDR is nominally between 30% and 40% DR [4,16–18]. Within the HDR regime (though below MDR), the classical view is that the mean velocity follows the ultimate profile [15] until the Newtonian plug, which once again has the same von Kármán coefficient (κ) value as that of the Newtonian flow.

While several experimental studies showed deviations from the classical view at HDR [10,16, 19–24], it was White *et al.* [25] who first re-examined this classical view and showed Direct Numerical Simulations (DNS) that do not support the classical results at HDR. Then, Elbing *et al.* [18] provided high Reynolds number experimental PDR TBL data that supported the findings of White *et al.* [25]. These deviations have also been extended to the LDR regime (see Ref. [26]), although the dependence is significantly weaker. Furthermore, Elbing *et al.* [18] showed that the deviations from the classical view could not be fully explained by variations in flow conditions or DR levels, which indicated that polymeric properties must impact the near-wall velocity profile. More recently, Elbing [27] reviewed the literature and made estimates of the local polymeric properties within a PDR TBL, showing that Weissenberg number (Wi) is the most likely polymeric property responsible for causing significant changes in the structure of the polymer-modified TBL.

Thus, the current study aims to experimentally examine the mean and fluctuating velocity profiles within a polymer-modified TBL with carefully controlled polymeric properties, particularly the Wi. The goal of the experiment was to create a developing TBL with known and *uniform* M_w and polymer concentration. This allows for clearly defining the polymeric properties of Wi, the ratio of the solvent viscosity to zero-shear viscosity, and the coiled-to-stretched length ratio within the TBL. This is typically not attempted because polymer degradation causes the M_w to change within the flow, which forces most experiments to inject high-concentration polymer at the wall that results in large concentration gradients within the TBL. This is especially true in the HDR regime, where the largest deviations from the classical view have been observed. However, combining the work of several TBL polymer degradation studies [14,28,29], the current work has been able to create multiple conditions with quasi-steady M_w within a TBL having a uniform concentration of polymer.

In terms of probing the flow physics, uniform polymer properties allowed for isolating the role of Wi and DR in shaping-up the polymeric flow statistics. Therefore, conditions were selected such that two conditions had nearly identical Wi with significantly different DR (15% versus 44%), and two others had nearly identical DR with significantly different Wi (0.2 versus ∼10). The friction-velocity-based Reynolds number (δ^+) was not exactly matched between conditions but was held to within the same order of magnitude. The effect of changes in δ^+ are emphasized as needed when comparing results. The remainder of the paper is organized as follows. Section II provides a detailed description of the experimental methods. Section III presents the results with an emphasis on separating the impact of DR and Wi. Section IV provides a discussion given the observed role of Wi. The article concludes in Sec. V.

II. EXPERIMENTAL METHODS

A. Test facility and model

Testing was performed in the Oklahoma State University 6-in. low-turbulence recirculating water tunnel [30]. The test section had acrylic walls for optical access and measured 1.1 m long with a

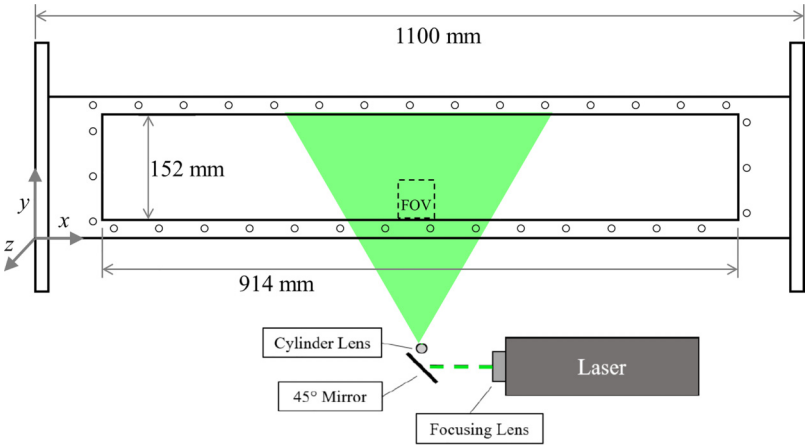

FIG. 1. Schematic of the PIV setup, including the laser, orientation of optical components, and the resulting FOV within the test section.

152-mm (6-in.) square cross section. A 112-kW (150 hp) motor (MP44G3909, Baldor) powered a centrifugal pump (S10B12A-4, Patterson), and a variable-frequency drive (EQ74150C, Teco) controlled the pump frequency to set the test-section flow speed. Flow conditioning (e.g., tandem configuration of honeycombs and settling chambers, 8.5:1 area contraction) resulted in an inlet turbulence intensity <0.3% and negligible mean shear within the test-section core. The total tunnel volume ($1.47 \pm 0.04\,\mathrm{m}^3$) was determined by comparing changes in conductivity (CDH-287-KIT, Omega Engineering) when adding known quantities of salt with an established calibration curve.

A boundary layer trip (uniformly distributed 122 μm grit) at the test-section inlet mitigated transitional effects on the tunnel walls. Measurements were acquired within the flat-plate TBL that formed on the test-section wall. The Newtonian (water only) coefficient of friction ($C_{f,N}$) on the wall was previously measured to be $C_{f,N} = 0.01565\mathrm{Re}_x^{-0.1086}$ [30], where $\mathrm{Re}_x = U_\infty x/\nu$ is the downstream distance (x)-based Reynolds number. Downstream of the boundary layer trip, the average surface roughness height (Ra) was at or below 0.8 μm. Converting Ra to Colebrook-type roughness (k_c) [31,32] and noting that the minimum viscous wall unit (l_v) was 7.5 μm, the maximum inner-variable scaled roughness height ($k^+ = k_c/l_v$) in the current study was $k^+ \leqslant 0.5$. Thus, the surface was considered hydraulically smooth. The coordinate system used throughout has the x origin at the test section inlet and extending in the downstream direction, the y coordinate increasing in the wall-normal direction with the origin at the tunnel wall (lower), and z extending in the spanwise direction completing a right-handed coordinate system.

B. Instrumentation

Particle image velocimetry (PIV) was used to acquire two components of the near-wall velocity vector field within the TBL. Two unique PIV setups were used to acquire either time-averaged or time-resolved vector fields. A time-averaged, two-dimensional (2D) PIV system in double-frame, double-pulse mode characterized the mean and fluctuating velocity profiles. The image plane was centered at $x = 0.53$ m and aligned parallel to the flow at the tunnel centerline ($z = 0$). The image plane was illuminated with a 532-nm Nd:YAG laser (Gemini200, New Wave, Fremont, CA) beam formed into a sheet with a nominal thickness of 0.7 mm. The light was scattered from 18-μm hollow glass sphere tracer particles (iM30K, 3M, Maplewood, MN), which was recorded with a 2560 pixels ×2160 pixels sCMOS camera (Imager, LaVision, Göttingen, Germany). Spatial calibration was performed with a high-precision calibration target (Type 58-5, LaVision, Göttingen, Germany). The nominal field of view (FOV) (see Fig. 1) was 49 mm (wall-normal) ×41 mm (streamwise).

The time-resolved PIV used high-speed measurements to investigate the near-wall turbulent structures. The image plane was centered at $x = 0.53$ m, aligned parallel to the flow, and on the tunnel centerline ($z = 0$). The image plane was illuminated with the beam of a high-speed Nd:YLF laser (DM30-527, Photonics) spread into an approximately 0.7-mm-thick sheet with a cylindrical lens as illustrated in Fig. 1. The same hollow glass spheres were used to scatter the laser light, which was now recorded with a high-speed camera (M110, Phantom) at a rate between 2 and 4 kHz, depending on the free-stream velocity. The high-speed camera had a maximum resolution of 1280 pixels $\times$800 pixels. The camera was fitted with a 60 mm diameter, f/2.8D lens (AF Micro NIKKOR, Nikon) that produced a nominal FOV of 10 mm (streamwise) $\times$15 mm (wall-normal). The images were calibrated with a 20 mm $\times$ 20 mm custom calibration target. The on-board camera memory allowed for a maximum of 6000 images to be acquired in a single sequence.

The PIV timing, acquisition, and image processing for both configurations were performed using a commercial software package (Davis 8.2.3, LaVision). The velocity vector fields were computed using standard multipass cross-correlation methods with decreasing interrogation window sizes (DaVis8, LaVision). The target final interrogation window sizes were 16×16 pixels with an overlap of 50% and 75% for averaged and time-resolved PIV, respectively. However, due to decreased particle density near the wall, the time-resolved windows at times had to be increased to 32×32 pixels with 75% overlap. The wall location was determined using mirrored particles at the wall, and the estimated uncertainty in the wall position was $\leqslant 30$ μm. The PIV uncertainty was quantified following the approach identified in Wieneke [33], which uses the asymmetry in the correlation peaks when slightly shifted ($\sim$1 pixel) away from the optimized displacement to quantify the impact of image noise, including out-of-plane motion. For the current study, the maximum uncertainty was ± 0.1 m/s ($\sim$0.3 pixels). Propagation of uncertainty for PIV-based statistics (e.g., Reynolds stresses) follows the analysis of Schiacchitano and Wieneke [34].

Other measurements included water temperature, static pressure, and pump motor frequency. The water temperature was measured with a T-Type thermocouple (TC-T-1/4NPT-U-72, Omega) located 0.92 m upstream of the contraction inlet. The static pressure was measured 76 mm upstream of the contraction inlet at the test section centerline elevation with a differential pressure transducer (PX230050DI, Omega) and the low-pressure side open to atmosphere. These measurements were recorded at 500 Hz throughout testing along with pump motor frequency from the variable frequency drive via a data acquisition card (USB-6218-BNC, NI) controlled with commercial software (LabView15.0.1, NI).

C. Polymer preparation and characterization

The polymer used in the current study was polyethylene oxide (PEO). PEO has a structural unit (monomer) of (–O–CH_2–CH_2–) that results in a polymer backbone consisting of carbon-carbon (C–C) and carbon-oxygen (C–O) bonds. Polymer batches were prepared with the manufacturer specified mean molecular weight (M_w) of 4×10^6 g/mol (WSR301, Dow Chemical) or 8×10^6 g/mol (Sigma-Aldrich) at concentrations between 1000 and 5000 ppm. The solutions were prepared by slowly sprinkling dry powder into a jet to prevent the formation of polymer aggregates. Trace amounts of sodium thiosulfate were used to mitigate polymer degradation due to background chlorine [11,35].

The fully hydrated, high-concentration polymer solution was diluted to a desired concentration in the water tunnel and allowed to uniformly disperse via molecular diffusion. Once fully mixed to produce a homogeneous polymer concentration (termed a polymer ocean), the water tunnel was operated at the test speed to produce a degraded, quasi-steady (i.e., negligible variation for periods of time longer than that required to record data) M_w. A detailed comparative analysis between mechanically degraded polymers within the polymer ocean and nondegraded samples at the same M_w was performed in a separate study [29]. Farsiani *et al.* [29] showed that significant deviations in performance can occur but also identified a range of operating conditions that had negligible difference between the degraded quasi-steady polymer ocean samples and the nondegraded samples

at the same M_w. The operation range for the current study was selected to coincide with the conditions that had negligible difference between degraded and nondegraded samples. Thus, the current study had a steady M_w during testing, and therefore, a nearly steady state M_w distribution. Here, it is important to note that the M_w of the polymer ocean was monitored via analysis of sample solutions taken from the tunnel at regular intervals throughout testing. In addition, each polymer ocean was prepared at least three times and the M_w variation was within $\pm 10\%$.

The M_w of a polymer ocean sample was determined from the shear rate at the onset of DR (γ^*), which is a well-established approach for estimating the M_w of PEO solutions [14,28]. Here, the onset of DR is identified from the intersection of the experimentally obtained polymeric friction curves with the friction law for the fully developed turbulent (smooth) pipe flow of a Newtonian fluid (i.e., the Prandtl–von Kármán law). Vanapalli *et al.* [28] compiled PEO data [3] to establish a relationship between γ^* and the M_w, $\gamma^* = 3.35 \times 10^9/M_w$. The pressure drop apparatus used to acquire the polymeric friction curves consisted of a precision stainless steel pipe with ports for measuring the pressure drop along the pipe length. A detailed description of the pressure drop apparatus is given in Farsiani *et al.* [29], and a detailed analysis of the measurement uncertainty is in Lander [36]. The overall uncertainty was determined by propagating the uncertainties associated with measurements of fluid temperature (used to determine water properties), pipe dimensions (e.g., diameter and length between pressure ports), pressure difference including the impact of the holes in the wall to make the pressure taps [37], and mass flow rate. The reader is referred to Farsiani *et al.* [29] for more on this uncertainty analysis. While the uncertainty of a single operation condition varied significantly, the resulting uncertainty in the M_w was $\sim 10\%$ [29,36].

The pressure drop apparatus was also used to determine the intrinsic concentration [C] and intrinsic drag reduction [DR] [38]. The intrinsic polymer properties have been used to establish a relationship between polymer concentration (C) and the resulting drag reduction (DR) [3,12,39,40],

$$\frac{DR}{C} = \frac{[C][DR]}{[C] + C_M}. \tag{1}$$

Choi and Jhon [40] showed that these intrinsic DR properties for solutions of PEO-water were universal regardless of the flow geometry (e.g., pipe versus boundary layer) and solvent. Thus, these intrinsic properties were used to estimate the DR with the polymer ocean relative to the Newtonian flow.

D. Test conditions

The average water temperature was $22.0^\circ\text{C} \pm 1^\circ\text{C}$ throughout testing, giving a corresponding average kinematic viscosity (ν) of $9.55 \times 10^{-7} \pm 2.3 \times 10^{-8}$ m^2/s. PIV was acquired at $x = 0.53$ m and at local free-stream speeds (U_∞) of 1.6 m/s and 3.3 m/s. For the Newtonian conditions, these had a corresponding nominal momentum thicknesses (θ) of 1.0 and 0.9 mm, respectively. The momentum thickness was determined by integrating the boundary layer velocity profile fitted with a power-law curve fit. The resulting momentum thickness–based Reynolds number ($\text{Re}_\theta = U_\infty \theta/\nu$) for the Newtonian conditions ranged from 1810 to 3310. These test speeds had a friction Reynolds number ($\delta^+ = u_\tau \delta/\nu$) of 700 and 1320, respectively. Here, δ is the 99% boundary layer thickness, $u_\tau \equiv \sqrt{\tau_w/\rho}$ is the friction velocity, τ_w is the wall-shear stress, and ρ is the fluid density. The friction velocity can be rewritten using the definition of coefficient of friction ($C_f \equiv \tau_w/(0.5\rho U_\infty^2)$ and drag reduction ($\text{DR} = 1 - \tau_{w,p}/\tau_{w,N}$),

$$u_\tau = U_\infty \sqrt{\frac{C_{f,N}}{2}(1 - DR)}. \tag{2}$$

Here, the subscripts N and p indicate Newtonian and polymer conditions, respectively. The coefficient of friction in the tunnel for Newtonian (water only) flow was determined in a previous study [30],

$$C_f = 0.015\,65 \text{Re}_x^{-0.1086}. \tag{3}$$

TABLE I. List of obtained test conditions with associated markers for each condition, which are used throughout the manuscript. Note that the Wi number reported here is based on the degraded M_w, given in the table above, of the sample tested; refer to Sec. II C for more details.

Condition Ref.	Re_θ	DR (%)	δ^+	U_∞ (m/s)	u_τ (m/s)	Wi	$M_w \times 10^6$ (g/mol)
N1, ○	1810	0	698	1.6	0.069	–	–
N2, ▷	3310	0	1320	3.3	0.132	–	–
P1, ▲	1560	15	585	1.6	0.064	0.2	0.7
P2, ■	1880	15	755	3.3	0.123	9.7	2.8
P3, ●	1550	44	474	3.3	0.100	13	4.2

The friction velocity uncertainty was calculated for each condition using standard propagation of uncertainty, but the average friction velocity uncertainty was 0.012 m/s.

The polymer ocean concentration was fixed at 100 ppm, and the steady-state M_w was varied between 0.7×10^6 and 4.2×10^6 g/mol. A total of three polymeric test conditions were selected, with the δ^+ ranging from 474 to 755. Note that two of these three conditions had the same DR of 15%, while one had a significantly higher DR of 44%. For these respective conditions, Weissenberg numbers ($\mathrm{Wi} = \lambda_p u_\tau / l_\nu$) ranged from 0.2 to 13. Here λ_p is the polymer relaxation time and $l_\nu (= \nu/u_\tau)$ is the viscous wall unit. See Table I, which summarizes the test conditions for both the polymeric and Newtonian flows. As pointed by a referee, the current values for DR and Wi are of the same order of magnitude as in the distributions given by some previous experiments [41]. However, the authors do not expect an exact match between values obtained herein and elsewhere because they are a function of the polymer type, which in turn sets Wi at the onset of DR values.

The relaxation time is dependent on whether the polymer solution is dilute. Polymer solutions are considered dilute when the concentration is below the overlap concentration, $C^* = 1/[\eta]_0$. Here, $[\eta]_0$ is the intrinsic viscosity, which was estimated from the Mark-Houwink relationship [42],

$$[\eta]_0 = 0.0125 M_w^{0.78}. \tag{4}$$

Thus, in the current study $C^* \geqslant 517$ ppm. This makes all of the polymer solutions dilute (i.e., separation between individual polymer chains is sufficiently large to have a minimal chain-to-chain interaction). The relaxation time for dilute polymer solutions can be estimated from the Zimm time [43],

$$\lambda_z = 0.422 \frac{[\eta]_0 \mu_s}{RT} M_w, \tag{5}$$

where R is the ideal gas constant and T is the absolute temperature.

The solvent (i.e., water) viscosity was used for the polymer solution viscosity within the turbulent boundary layer. Kalashnikov [44] studied the viscosity of dilute PEO solutions and found that the viscosity approaches that of the solvent when the shear rates are above $\sim 1000\,\mathrm{s}^{-1}$. The minimum wall-shear rate in the current study was $\sim 4000\,\mathrm{s}^{-1}$. In addition, the current study was tested at a relatively low concentration (100 ppm), where rheometer measurements confirm that the difference between the solvent and solution viscosity was minimal at low concentrations. Other critical nondimensional polymer-dependent parameters include the ratio of the solvent viscosity to the zero-shear viscosity of the polymer solution (μ^*) and the length ratio of the fully extended to coiled polymer molecules (L). These parameters had minimal variation in the current study with the ranges of μ^* and L being 0.93–0.99 and 125–308, respectively. The attained conditions, with their key indicators, have been summarized in Table I.

E. Proper orthogonal decomposition (POD) analysis

Proper orthogonal decomposition (POD) is a method of reduced-order modeling that involves decomposing an ensemble of given fields (velocity in the current study) into spatial modes (basis functions) modulated by a basis-function coefficient. The modes are ordered such that the first mode identifies the motions with the most energy on average, with each subsequent mode associated with less energetic motions. While widely used for a variety of problems, POD in the context of turbulent flows was pioneered by Lumley [45]. As commented by Berkooz *et al.* [46], the remarkable thing about POD is its linear nature and that it can be applied to a nonlinear problem without having to make the simplifying assumptions that may linearize the problem itself. The mathematical formulation of POD is not provided here, as it is a well-established approach; see, e.g., Pope [47]. The current study follows the POD procedures in Wu [48], though applied to both Newtonian and polymeric TBL flows. In general, the current study decomposed the instantaneous realizations of the fluctuating velocity field measured with PIV within the x-y plane into an infinite series comprising the product of spatial modes and temporal coefficients. This was then posed as an eigenvalue problem to identify and link the structural flow features making the most dominant contributions to the flow statistics.

III. RESULTS

A. Mean velocity profiles

The time-averaged streamwise velocity profiles for the two Newtonian conditions (N1 and N2 in Table I) are scaled using inner variables in Fig. 2(a). The profiles were resolved to within $y^+ = 50$ for the lowest Reynolds number tested. For each condition, three independent velocity profile measurements were acquired. The free-stream velocity uncertainty was ∼0.0048 m/s, as determined from twice the standard deviation from multiple profiles at the same condition. The Newtonian results from De Graaff and Eaton [49], spanning the current range of δ^+, are also included in Fig. 2(a) for reference. The classic log-law ($\kappa = 0.40$, $B = 5.0$) curve falls between the current results and those in De Graaff and Eaton [49]. The difference between experiments is likely due to slight differences in the local pressure gradients, since high-Reynolds-number findings suggest that even mild pressure gradients can alter mean velocity profiles [50,51]. The slope of the current log-layer results are in good agreement with the law-of-the-wall within the overlap region, which was identified using the indicator function ζ ($= y^+ \, du^+/dy^+$). For the log layer, this is the region of nearly constant ζ.

The inner-variable scaled, mean streamwise velocity profiles for the polymeric conditions (P1, P2, and P3 in Table I) are shown in Fig. 2(b). For comparison, the current Newtonian results (N1 and N2) are included, as well as the log-law curve and the ultimate profile for polymer drag reduced flows [15]. Several well-established features (see Refs. [12,16,18,52]) are observed in Fig. 2(b): (i) the inner-variable scaled log-layer shrinks with increasing DR; (ii) the log-layer intercept constant B increases with increasing DR for LDR (i.e., DR $\leqslant$ 35%); and (iii) while κ remains nearly constant at its Newtonian value for lower drag reduction levels (P1 and P2), it decreases for the HDR condition (P3). Clearly, the universality observed for the mean Newtonian profiles is lost with the addition of the drag-reducing polymers. Hence, a simple inner-variable scaling is insufficient to collapse polymeric results in a manner similar to the Newtonian flows. In addition, attempts to scale the profiles using DR and Reynolds number have proven to be insufficient, as shown by Elbing *et al.* [18]. This indicates that polymeric properties must also be influencing the mean statistics. Recent evidence [27] indicates that the Weissenberg number, Wi, is the key polymeric parameter influencing the mean statistics.

A critical difference between the current results and those previously used to examine the influence of Wi on developing TBL is that the current study produces *known and uniform* Wi values. Nearly all past PDR TBL studies have injected highly concentrated polymer solution upstream, producing streamwise and wall-normal concentration gradients throughout the TBL. This

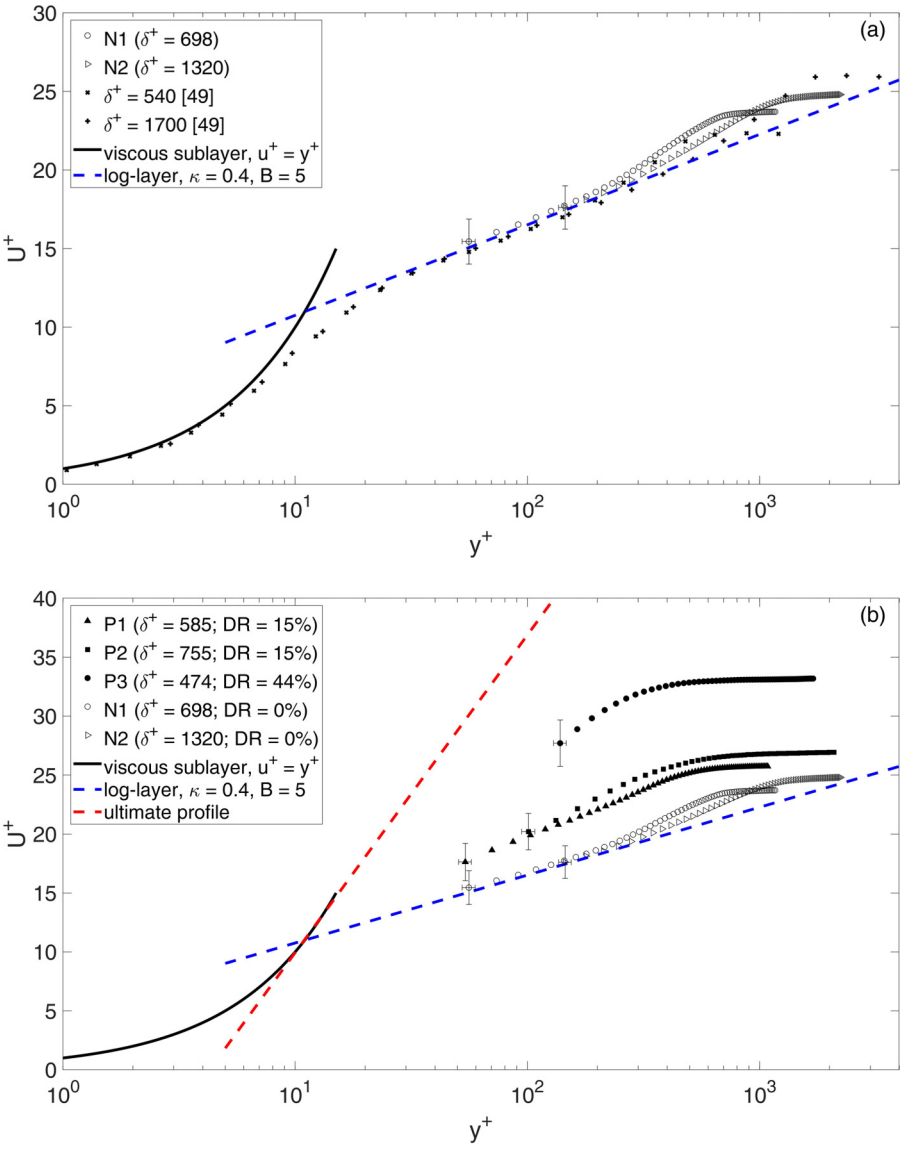

FIG. 2. (a) Time-averaged, Newtonian streamwise fluctuating velocity profiles, and (b) time-averaged, polymeric mean profiles. Refer to Table I for more details on the figure legend. For each profile a representative error bar is included that is equal to the mean uncertainty for that profile within the boundary layer.

is in addition to the likely unaccounted-for changes in the molecular weight due to shear-induced polymer degradation [14]. These results confirm that the level of DR is the primary parameter setting the shift in the log-layer (e.g., N1 and P2 have similar δ^+, and the two curves look extremely similar with the P2 condition simply shifted upward). In addition, the secondary impact of Wi is observed with a small change in the log-layer slope between conditions P1 and P2, which have the same DR level and same order of magnitude δ^+. This is nominally consistent with previous observations in Ref. [27], where increased scatter in the κ values were observed for DR $\gtrsim$15%. While P3 has a truncated log-layer, the general trend of P3 having a larger slope (i.e., smaller κ) is observed. However, Elbing [27] indicates that for previous experimental TBL studies $\kappa \sim 0.32 \pm 0.05$ for

DR = 44% and Wi ≈ 13, but for P3 $\kappa \sim 0.2$. While this could be the result of flow-field changes associated with the uniform polymer solutions, the most likely cause is the lack of resolution at this higher drag reduction condition.

B. Fluctuating velocity profiles

The velocity field in a TBL is set up by the relevant eddies via the Biot-Savart law. Therefore, the instantaneous wall-shear stress is the superposition of what is termed as the active and inactive part of the motions induced by such eddies [53,54]. Given this, the mean flow observations indicate that polymers preferentially target these eddies. So, the statistical structure of the modified fluctuating velocity field in polymeric flows provides further insights into the PDR mechanism. Of note, a very high Reynolds number [$\mathrm{Re}_\theta \sim \mathcal{O}(10^4)$] is required to obtain the required scale separation to statistically realize inactive vortical motions. This was not possible in the current study, because polymer rapidly degrades at higher flow speeds, preventing the identification of a stable condition with sufficiently high Wi and DR [14,29]. Consequently, the trends observed in the current study are likely linked to the polymer-effected active vortical motions only.

The inner-variable scaled profiles for the Newtonian streamwise component of turbulent kinetic energy (TKE) are compared with previous results at a similar range of δ^+ from De Graaff and Eaton [49] in Fig. 3(a). Once again, the trends between the current Newtonian conditions and those of De Graaff and Eaton [49] are consistent, which supports the accuracy of the current fluctuating profile measurements. Following this, the current Newtonian and polymeric conditions are compared in Fig. 3(b). The stark change in the profile structure is readily apparent, which indicates a morphologically altered flow when polymers are added. The significantly higher scaled values for the polymeric conditions in Fig. 3(b) are somewhat misleading, because the apparent increase in $\overline{u'^2}^+$ is primarily due to the decrease in u_τ rather than an increase in the fluctuation magnitudes. The streamwise velocity fluctuation magnitudes (nonscaled) for conditions P2 and P3 at $y^+ < 200$ were nearly identical, in spite of the apparent difference observed in Fig. 3(b). Note that these conditions have nearly identical Wi with a significantly different δ^+. By comparing conditions N1, P1, and P3 (see Table I for more details) it was *ascertained* that streamwise fluctuations increase only marginally in magnitude with increasing Wi. It also appears that for the HDR condition (i.e., condition P3), the streamwise fluctuations sharply decrease to levels lower than those obtained with either of the other conditions for outer regions of the TBL.

The inner-variable scaled profiles for the wall-normal component of TKE are plotted in Fig. 4. Once again, the baseline Newtonian results are compared with conditions from De Graaff and Eaton [49] spanning the same δ^+ range in Fig. 4(a). The current Newtonian profiles are consistent with the trends observed in De Graaff and Eaton [49]. Conversely, Fig. 4(b) provides a comparison between the current Newtonian (N1 and N2) and polymeric (P1, P2, and P3) conditions, which shows that polymer causes a strong suppression of the wall-normal velocity fluctuations. The level of suppression for the wall-normal fluctuations appears to primarily depend on Wi, as P1 and P2 have the same DR level (15%) at similar δ^+ but the wall-normal suppression is significantly larger for P2. Furthermore, the suppression in P2 is nearly identical to that in P3, which has a higher DR (44%) but nearly identical Wi. Note that the observed suppression in the scaled profiles reflects an even larger suppression of the nonscaled wall-normal velocity fluctuation magnitudes given that the polymer is also decreasing u_τ. Combining this observation with the lack of suppression in the streamwise component, it reflects the increase in anisotropy due to the addition of polymer. Thus, the trending anisotropic fluctuating velocity field observed for lower δ^+ polymeric TBL [16,52] is extended to higher δ^+ polymeric TBL with potential dependence on Wi.

The near-wall exchange of momentum effects drag at the wall and is connected to the Reynolds shear stress, which is examined next. As before, the inner-variable scaled Newtonian Reynolds shear stress is first compared with results from De Graaff and Eaton [49] spanning the current δ^+ range in Fig. 5(a). The current results are bracketed between the curves from De Graaff and Eaton [49] for nearly all measured y^+ locations. Figure 5(b) shows that the Reynolds shear stress is relatively

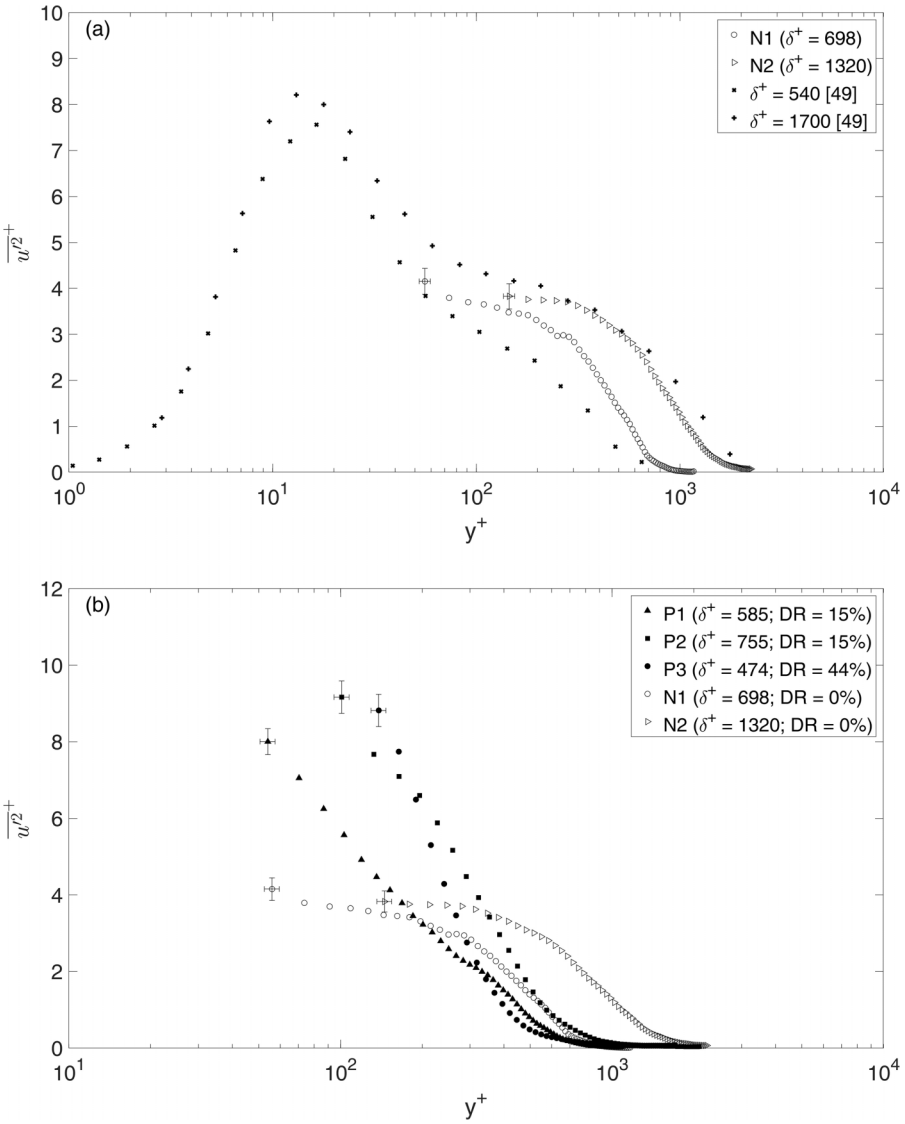

FIG. 3. (a) Newtonian and (b) polymeric inner-variable scaled streamwise fluctuating velocity profiles. Refer to Table I for more details on the corresponding operation conditions. For each profile a representative error bar is included that is equal to the mean uncertainty for that profile within the boundary layer.

muted when compared with the Newtonian conditions, though it is not as severe as that observed for the wall-normal fluctuations. This suppression appears to depend on Wi, which is clearly observed upon comparing condition N1 with P2 and condition P1 with P3. These conditions have the same order of magnitude for δ^+ but a markedly different Wi (see Table I). The suppression increases with increasing Wi, with a stronger dependence than that of DR (i.e., P1 and P2 have the same DR with significantly different suppression). However, it is also apparent that the suppression is not only dependent on Wi, which can be seen by comparing conditions P2 and P3. Here, the curves are similar but shifted relative to each other in a manner similar to that observed in Fig. 5(a), which suggests that this shift is related, in part, to the parametric dependence on δ^+. Thus, a larger scale separation facilitates intense Reynold shear stress to register higher drag. Therefore, the degree of

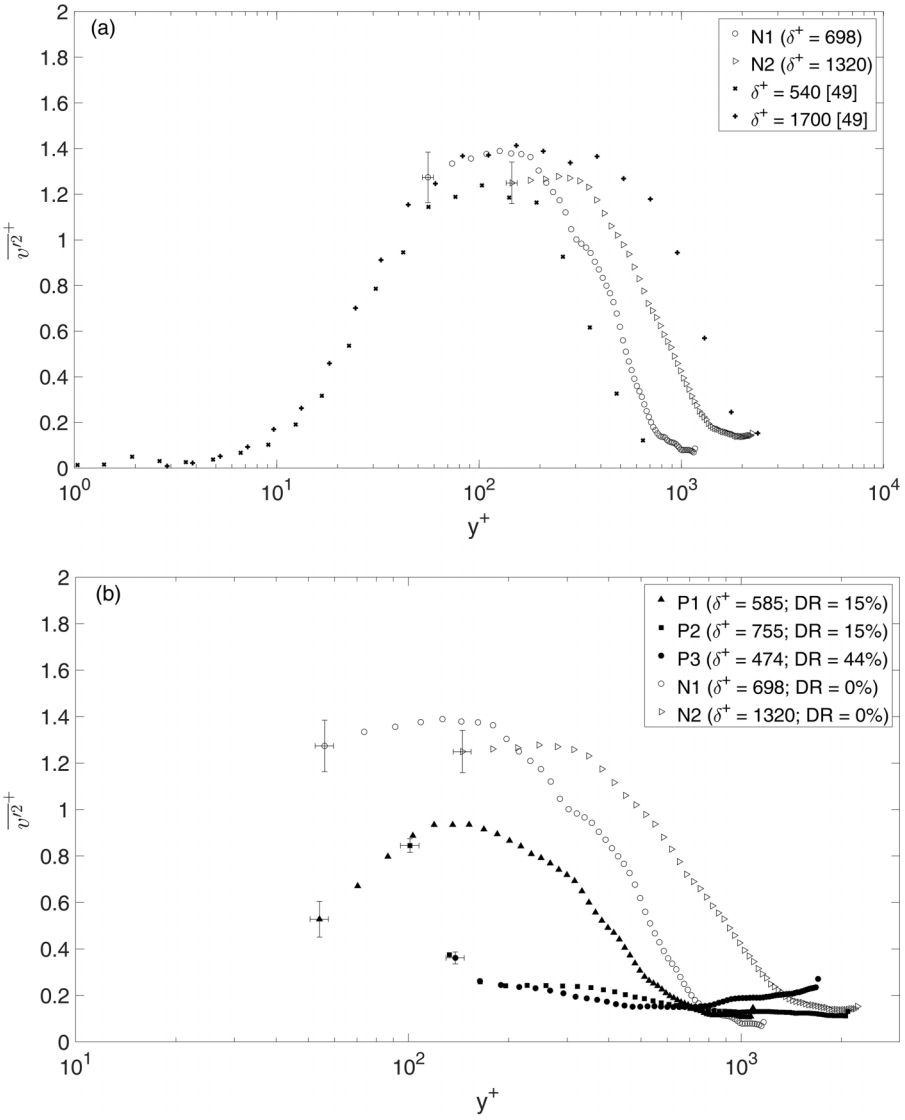

FIG. 4. (a) Newtonian and (b) polymeric inner-variable scaled wall-normal fluctuating velocity profiles. Refer to Table I for more details on the corresponding conditions. For each profile, a representative error bar is included that is equal to the mean uncertainty for that profile within the boundary layer.

separation between the flow length scales and the extent of stretch induced upon polymer chains by such scales of the motion play an antagonistic role in the near-wall transfer of momentum for polymeric flows.

C. Conditional averaged Reynolds shear stress profiles

To further investigate the impact of polymer additives on specific coherent structures, the inner-variable scaled Reynolds shear stress values were conditionally averaged to isolate ejection (Q_2) and sweep (Q_4) events for each polymeric condition tested. The conditional averaging was performed using quadrant-based analysis [55], where every vector from each PIV snapshot was sorted based on

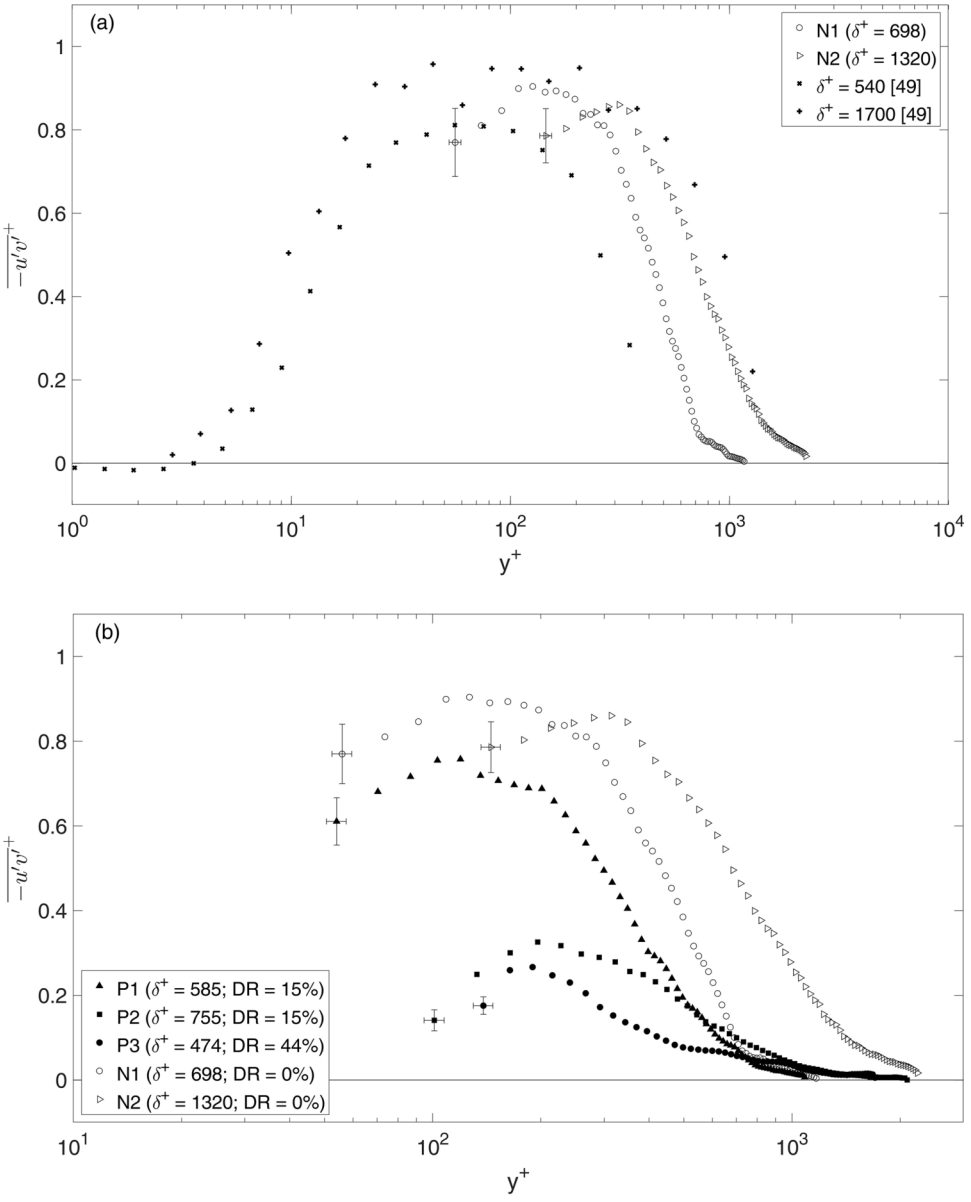

FIG. 5. (a) Newtonian and (b) polymeric inner-variable scaled Reynolds stress profiles. Refer to Table I for more details on the corresponding operation conditions. For each profile a representative error bar is included that is equal to the mean uncertainty for that profile within the boundary layer.

the quadrant for the fluctuating velocity components. Specifically, a positive (negative) streamwise velocity fluctuation when paired with a negative (positive) wall-normal velocity fluctuation was classified as a sweep (ejection) event. The conditionally averaged Reynolds shear stress profiles for the ejection and sweep events are shown in Figs. 6(a) and 6(b), respectively. The conditionally averaged results for the Newtonian conditions are also included for comparison. The first observation is that for all conditions, the peak scaled value is nominally twice as large with the conditionally averaged events (sweep and ejection) relative to the full profiles in Fig. 5. This is consistent with

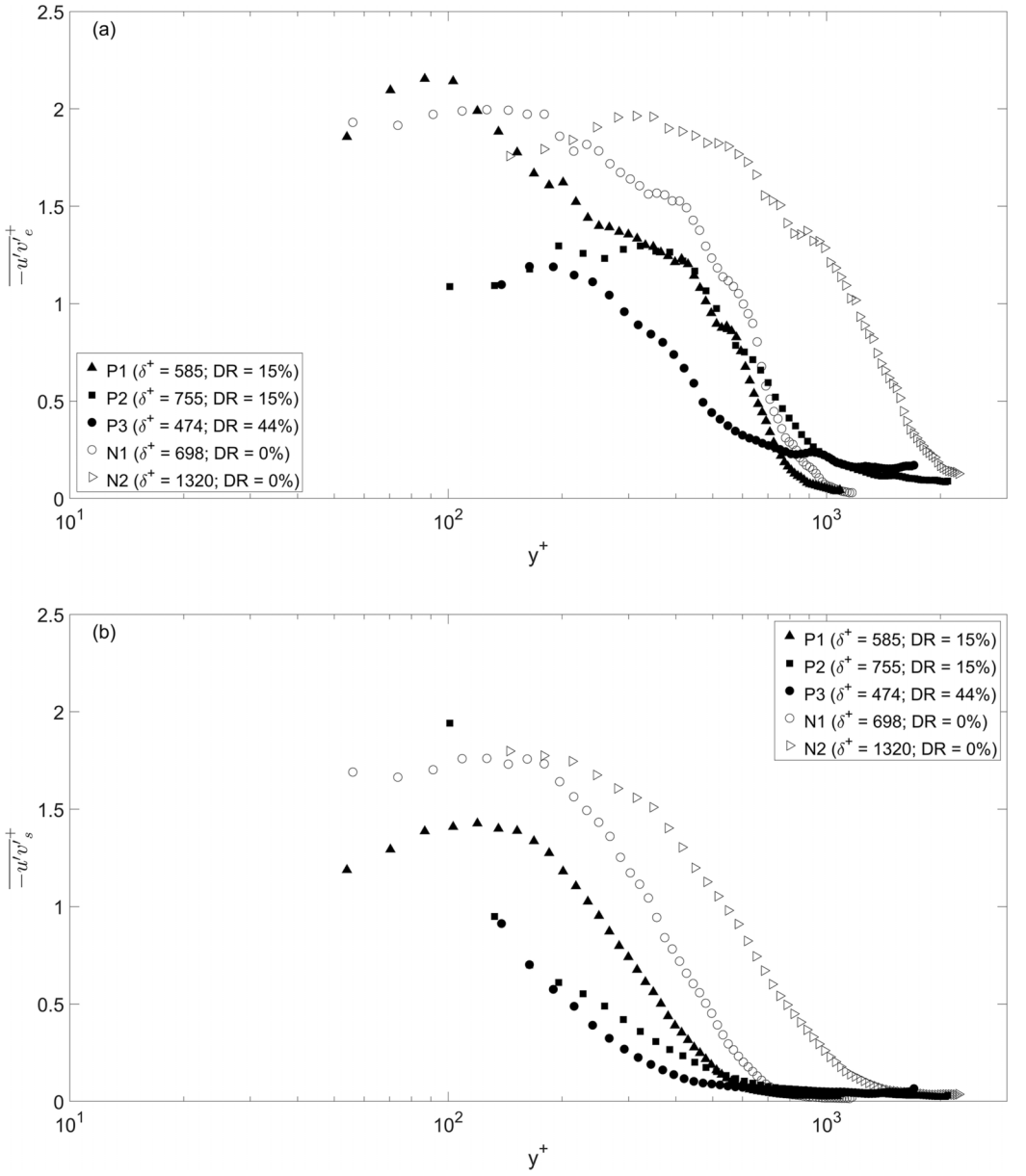

FIG. 6. Inner-variable scaled Reynolds stress profiles conditionally averaged to identify (a) ejection and (b) sweep events for Newtonian and polymeric conditions. Refer to Table I for more details on the corresponding operation conditions.

the notion that most of the fluctuating energy is associated with these events (i.e., the sweep and ejection contribute positively to the overall Reynolds stress balance). In addition, the δ^+ dependence is readily observed in both the ejection and sweep events by comparing the Newtonian conditions (N1 and N2), which are the same conditions (i.e., DR $= 0\%$) apart from the differences in Reynolds number.

Focusing on conditions N1, P1, and P2 provides insights into the Wi dependence on ejection and sweep events. These conditions have similar δ^+ values with significantly different Wi values that

range from 0 (Newtonian) to 9. The ejection events in Fig. 6(a) show minimal variation between conditions in the outer region of the TBL, but the curves diverge in the near-wall region for $y^+ \lesssim 300$: over the range of $100 < y^+ < 300$, the general trend is that the ejection fluctuations are suppressed with increasing Wi. For instance, when conditions N1 ($\delta^+ = 698, Wi = 0$) and P2 ($\delta^+ = 755, Wi = 9$) are compared, the maximum suppression is nearly 50% relative to the condition N1 for a fixed $y^+ = 100$. However, for $y^+ > 200$, the suppression progressively decreases. For P1 with $y^+ \lesssim 100$, the ejection-related fluctuations exceed those of the Newtonian conditions, but for P2 the lack of near-wall resolution prevents an assessment of the trends within that range [see Fig. 6(a)]. For conditions with δ^+ in roughly the same range (i.e., conditions N1, P1, and P2), the sweep events in Fig. 6(b) have a simpler behavior, with the suppression increasing with increasing Wi throughout the entire TBL thickness. In general, polymers suppress the sweeping motions more strongly than ejection. For this, compare the sweeping and ejecting motions for conditions P1, P2, and P3 individually, in the range $y^+ > 100$. For P1 the sweeping motions are suppressed by a maximum of 30% relative to the ejecting motions; for P2 the sweeping motions are suppressed by a maximum of 50% relative to the ejecting motions; and for P3 the sweeping motions are suppressed by a maximum of 50% relative to the ejecting motions.

It is also instructive to compare the behaviors of P2 and P3, which have nearly identical Wi values with significantly different δ^+. The difference in δ^+ can explain the relative shift in the outer regions of the TBL with these shifts and their intersection in the near-wall region mimicking that observed in the Newtonian conditions (N1 and N2). Near the wall, in the region of $100 < y^+ < 200$, these polymer conditions (P2 and P3) have nominally equal scaled values for the ejection events, but the corresponding absolute values show that P3 (DR = 44%) was about 51% less for P2 (DR = 15%). A similar observation is valid within this region for sweeping motions. Thus, this shows that the impact of DR is accounted for with the inner-variable scaling, while both Reynolds number (δ^+) and Wi prevent the profiles from being universal.

D. Proper orthogonal decomposition mode distribution

The overarching theme of the results presented thus far is that polymer chains suppress fluid motions and hence the strength of the structures inducing such motions. In the absence of polymer chains, such motions facilitate the transfer of momentum to register higher drag. From the viewpoint of the spatiotemporal dynamics of such suppressed structures, the polymeric flows are expected to have a reduced structural complexity (i.e., the range of structures actively contributing to the instantaneous flow field are expected to be condensed). In some sense this is implied when the current interpretation of δ^+ is used in conjunction with the phrase *reduction in drag*. POD analysis, a form of reduced-order modeling, is a robust tool to examine the structural complexity of the flow. The POD modes provide spatial distributions that are ordered (ranked) by the level of TKE associated with the mode. This allows such modes to evaluate the distribution of TKE as a function of the energetic scales of motion, which are heavily influenced by the flow structures. Hence, the number of modes required to attain a given threshold of cumulative energy is commensurate with the range of structures that are, in general, contributing to the TKE.

The cumulative TKE is plotted versus the POD mode number for conditions N1 and P3 in Fig. 7. For clarity, only N1 and P3 are compared in this section, which were selected to span the range of Wi and DR tested (cf. Table I). For reference, a dashed line marking the 90% cumulative TKE threshold is included in Fig. 7. The Newtonian (DR = 0%, Wi = 0) and polymeric (DR = 44%, Wi = 13) conditions required 165 modes and 65 modes, respectively, to achieve the 90% threshold. Regardless of the threshold level selected, the Newtonian flow always required a larger number of modes relative to the polymeric flow. The difference in cumulative TKE between the polymer and Newtonian conditions at a given POD mode was largest for the first mode and progressively decreased with increasing mode number. The decreasing difference is expected, given that an infinite number of modes would perfectly replicate (i.e., 100% of the energy captured) both flow fields.

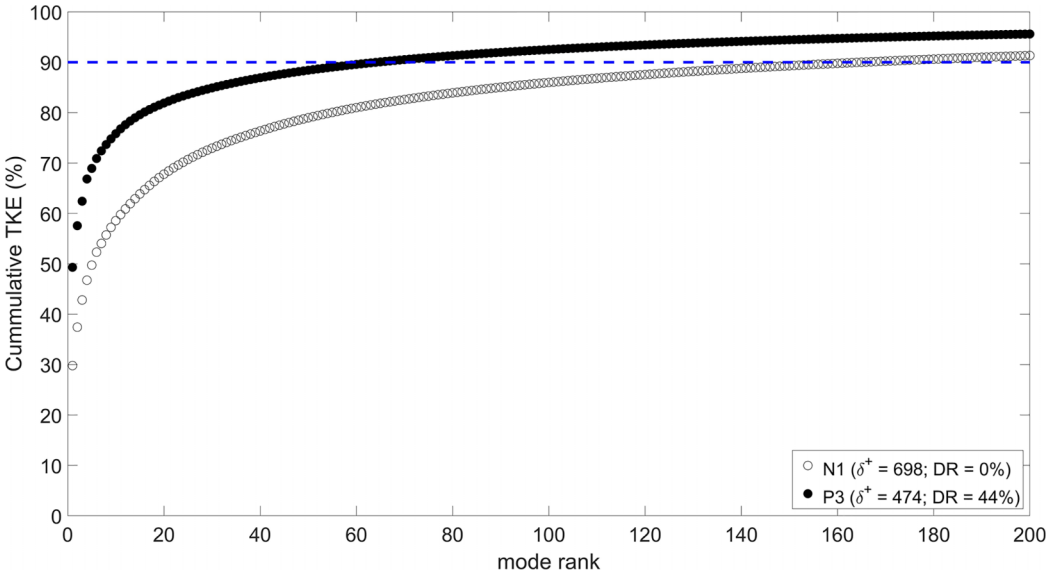

FIG. 7. Percent cumulative TKE vs number of POD modes for N1 (DR = 0%, Wi = 0) and P3 (DR = 53%, Wi = 53). Refer to Table I for more details on the corresponding operation conditions.

Table II provides the fractional energy associated with the first eight POD modes for conditions N1 and P3. This shows that nearly half of the cumulative kinetic energy (49.3%) was captured in the first mode for P3, but the Newtonian condition captured less than a third of the total cumulative kinetic energy in the first mode. This is also apparent in Fig. 7 by comparing the first data point for each condition. It indicates that the majority of the energy is contained within fewer structures in polymeric flow (P3) relative to the more broadband distribution among the scales of motions in the Newtonian condition (N1). This trend was observed regardless of which polymeric or Newtonian conditions are compared. For example, the use of condition N2 only further increases the complexity for the Newtonian condition due to the larger δ^+ (i.e., 195 modes are required to hit the 90% threshold). Note that while N1 and P3 have a difference in δ^+, P2 has a nearly identical δ^+ with N1 and the reduction in complexity is even greater than P3 (i.e., a 90% threshold was achieved with 31 modes for P2). This illustrates that while DR certainly reduces the complexity of the flow, it is the Wi that has a stronger correlation. For example, P1 and P2 were at the same DR level (15%) with P2 at a higher Reynolds number, but P2 with a higher Wi had less complexity (31 modes for 90% threshold) than P1 (77 modes for 90% threshold). These differences between conditions are all suggestive of a readjustment of the TKE, in terms of scales of motion operating to shape the velocity field, which is strongly associated with Wi. Since Wi is a ratio of the polymeric relaxation time to

TABLE II. Fractional energy distribution of the first eight POD modes for Newtonian (N1) and polymeric (P3) flows. Refer to Table I for more details on the corresponding operation conditions. $\Delta = n_{P3} - n_{N1}$ is the difference in energy in each mode between P3 and N1.

	Energy (%)							
Mode (n)	1	2	3	4	5	6	7	8
P3 (DR = 44%)	49.3	8.3	4.8	4.4	2.1	2	1.5	1.3
N1 (DR = 0%)	29.8	7.6	5.4	3.9	3	2.6	1.7	1.7
$\Delta = n_{P3} - n_{N1}$	19.5	0.7	–0.6	0.5	–0.9	–0.6	–0.2	–0.4

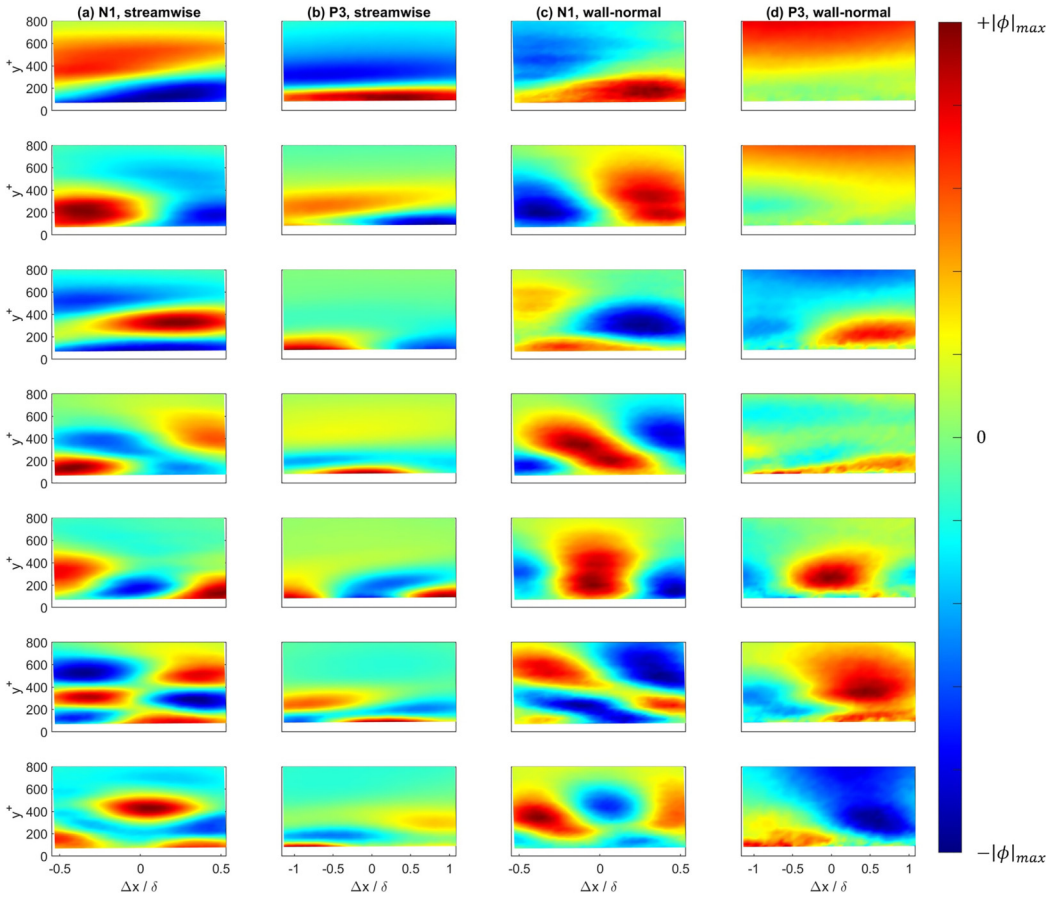

FIG. 8. POD modes 2 (top row) through 8 (bottom row) of the streamwise (a), (b) and wall-normal (c), (d) velocity components for N1 (a), (c) and P3 (b), (d) conditions. The spatial (streamwise) distances are scaled with the boundary layer thickness δ. Refer to Table I for more details on the corresponding operation conditions.

the timescales of the smallest scales of motion, this supports the view that when polymer chains are imposing their timescale dynamics on the flow they are, in essence, sensibly and actively rerouting flow energetics to achieve DR. This affects the structural complexity of the flow. Consequently, a smaller range of scales of motion contribute to the TKE in polymeric flows in proportion to the Wi for a given Reynolds number.

The spatial reconstructions of the streamwise and wall-normal velocity fields for modes (ϕ) 2–8 are provided in Fig. 8 for conditions N1 and P3. The decreasing flow length scales with increasing mode number shows that higher POD modes are associated with smaller scale coherent structures. Comparison between N1 and P3 of the wall-normal POD modes shows a reduction in the spatial density for the polymeric condition relative to the Newtonian case. In addition, comparison of the streamwise POD modes shows the polymeric condition elongated in the streamwise direction relative to the Newtonian condition, which is consistent with the enhanced correlations over larger streamwise length scales reported in Farsiani *et al.* [56]. The structures represented by the highest energy modes, as shown in Fig. 8, tend to have a progressively sparse distribution in space for the polymeric flow. Also, observe that the regions conducive to the generation of shear-layer instability (i.e., regions close to zero magnitude for the mode distribution) are less densely distributed. This

indicates that the variations in the velocity statistics for such regions are milder for the polymeric flows, as compared to Newtonian flow. In other words, owing to a scant distribution of the structures, the shear-layer instabilities are also milder. This in turn would prevent the formation of offspring structures, because the parent primary structures approach each other less frequently, in a less-closely-packed configuration. In conjunction with the countertorques provided by the polymers [57], this is a manifestation of conditions that are less propitious for a dense spatial distribution of structures, as observed in Fig. 8.

IV. DISCUSSION: INTERPRETATION USING FLOW AND POLYMER PHYSICS

The current results demonstrate that polymers reduce the complexity within a TBL, both in terms of the structures and their induced motions. The key observations are (i) enhanced anisotropy in the fluctuating velocity field, (ii) muted ejections and sweep events, and (iii) readjustment of the turbulent kinetic energy (TKE) among the relevant scales of motion as shown by the POD modes. Furthermore, control of the polymer properties produced a clear experimental demonstration that these statistical trends are Wi dependent, which supports recent TBL observations (see, e.g., Ref. [27]). Thus, in light of these results combined with established literature, several implications of the polymer chain action (and its connection to the Wi) on the flow structures within a developing TBL are further discussed.

Innate to wall-bounded turbulent flows is their ability to distribute the TKE streamwise component in the wall-normal and spanwise directions. This is achieved via the nonlinear inertial interactions involving the pressure-strain term as well as the Reynolds stress-fluctuating vorticity correlation terms in the underlying TKE budget equation. Physically, Offen and Kline [58] proposed that it could be due to the vortical interaction during their breakage as they commit to the downscale transfer of energy in the turbulence cascade. A growing degree of anisotropy indicates that the polymer chains modulate this energy transfer by limiting some of the key mechanisms (or motions) in this process. The polymer chains mitigate this energy transfer process via the turbulence cascade, resulting in the flow being more aligned in the streamwise direction and ultimately reducing the drag. Therefore, the mechanisms in effect for the cross-stream transfer of momentum (i.e., movement towards or away from the wall) in Newtonian flows are progressively subdued by the polymers.

The ejection and sweep motions play a significant role in momentum exchange within a TBL. Morphologically, such motions are achieved via the hairpin-type vortex structures (HPV) inhabiting near-wall regions. HPV induce destabilizing motions that impinge upon the near-wall momentum-deficit streaks (see Refs. [58,59]). Such motions culminate in sweep, ejection, and burst events (see Refs. [60,61]) that positively contribute to the overall Reynolds stress balance. As shown in Fig. 6, weakened ejections and sweep events indicate that such HPV are modulated by the polymer chains. Given Robinson [62], this suggests that the near-wall HPV must be altered in geometry, orientation, position, and swirl strength to reduce drag. Kim *et al.* [57] showed that polymer chains modulate such HPV by providing countertorques that weaken the near-wall HPV, which results in suppressed ejection and sweep motions. Furthermore, a reduced wall-shear stress, by definition, corresponds to a reduced spatiotemporally averaged drag over regions bearing the stress minima and maxima imprints at the wall [63]. In particular, the sweeping motions are expected to play a key role in determining wall-ward motions of the underlying HPV. The reduced wall-normal velocity fluctuations suggest that the wall-ward traveling structures not only approach it at a shallower angle [56,64] but also have reduced momentum. This registers a lower overall, spatiotemporally averaged wall-shear stress. Therefore, given the correspondence between sweeping motions and the wall-shear stress, it is natural to connect the observations from Fig. 6(b) to the question of *how polymers reduce drag*.

Given the literature (e.g., Refs. [58,59,65]), it is also instructive to analyze the reduced intensity of ejections [see Fig. 6(a)] within the context of the events that induce them. As mentioned, HPV plays a crucial role is self-sustaining the near-wall cycle of turbulence, which includes inducing

adverse pressure gradients that destabilize the near-wall streaks [59]. Consequently, the polymers, via the production of countertorques on these HPV [57], must also weaken the destabilizing motions that these structures produce, which aid in the transfer of momentum. Prior PDR TBL studies have statistically shown that bursting events have a reduced temporal frequency in polymeric flows [20,66]. This indicates that the near-wall streaks maintain their integrity over larger spatiotemporal scales. Therefore, by virtue of the weakened flow structures, polymer chains also contribute to stabilize the turbulence-promoting motions in the near-wall region.

Weakened flow structures could also provide an explanation for the dynamically different separation of the scales of motion between the polymer and Newtonian flows. For example, the polymeric countertorques [57] should impact the scales of motion contributing to the turbulence spectrum. Implicit in this is the readjustment of the TKE distribution across the various scales of motion. Consider this scenario by first noting that δ^+ is a measure of the range of active scales. The significantly reduced number of POD modes required to capture a given TKE level for polymeric flows hints at a significant drawdown of the structures in terms of their spatiotemporal frequency as well as their swirl strength. Ordinarily (i.e., without polymers), when the Reynolds number is sufficiently high the flow readily amplifies minuscule perturbations to develop a complex structural hierarchy (i.e., the "forest" of structures in a TBL [67]). Now, fewer POD modes required to capture the TKE indicates a condensed range of structures that can meaningfully influence and shape the fluctuating flow field. As delineated above, polymers selectively act on flow structures based on their swirl strength (or the eddy turnover times when discussed in reference to Wi—the ratio of stretch-relax cycle timescale to the flow timescales). A reduced complexity in the overall distribution of flow structures indicates that the offspring-shedding mechanism of the coherent structures has been mitigated. Based on the findings of Zhou *et al.* [68], the ability of a parent structure to shed an offspring depends if its inherent swirl strength is above a threshold. Therefore, the birth of offspring structures hinges on the swirl strength of the parent structure being sufficient to instigate a shear-layer-type instability. Given that polymers provide antitorque to restrict flow structures [57], it is natural to conclude that polymer chains inhibit their swirl strength and therefore their ability to shed offspring structures.

Given the POD mode analysis (Fig. 7), it is expected that polymeric flows have less densely packed structures, which is supported by the significantly larger TKE within the first mode (49% for P3 versus 30% for N1; cf. Table II). This suggests that polymer additives preferentially inhibit the high-frequency content, which is consistent with recent experimental work decomposing the scales of a PDR TBL [69]. Given the demonstrated importance of Wi, the selective action can be explained based on the differences in timescales for high- and low-frequency flow structures. Due to the stretch-relax cycle of the polymer chains, it is expected that the high-frequency structures are more likely to keep the polymer chains stretched, which allows them to impact the velocity fluctuations in the form of viscoelastic stresses. This scenario is less likely with low-frequency structures because they are not strong enough to keep the polymer chains stretched for such long periods. Hence, the low-frequency structures are more likely to evade the action of polymer. This is in line with the polymer-induced modified stress distribution put in perspective of the turbulence cascade theory by Tabor and De Gennes [70]: Polymer additives truncate the turbulence cascade at a certain scale where the elastic stresses are comparable to the local Reynolds stresses. Therefore, it is consistent to observe that the high-frequency flow structure is preferentially subdued, if not switched off, by the polymer additives. This is consistent with previous observations of polymers impact on two-point correlations in polymeric flows [56].

Finally, these observations are discussed in light of the conclusions drawn in earlier studies [27]. The current experiments indicate that the extent to which turbulent motions are mitigated in polymeric flows depends on how fast such scales of motions evolve relative to the timescale of the polymer chains (i.e., Wi dependence). Therefore, the ability of flow structures to generate offspring in polymeric flows is linked to Wi. In this regard, a subtle issue is that it is not the range of structures (i.e., the relative size between the largest and the smallest flow scales) that holistically determines the PDR TBL flow. Instead, the way the energy is distributed among the dwelling

structures also contributes towards determining the characteristic properties of a polymer-modified TBL (e.g., wall-shear stress, fluctuating flow field, and TKE distribution). In the authors' opinion, this is because polymers allow the energy distribution among the various flow scales to be different due to additional physics (enforced by the polymers) that upholds the flow. Note that the acting principle of PDR is their ability to cyclically stretch and relax due to the motions induced by the flow structures [45]. This underpins the fact that Newtonian and polymeric flows with the same large-scale forcing (e.g., free-stream velocity) can exhibit vastly different flow characteristics (refer to Fig. 7 comments comparing conditions N2 and P3 and the results presented in Sec. III). This suggests that the polymer-modified flow properties depend on how fast the scales of motion evolve relative to the inherent ability of the polymer chains to relax. Had this not been the case, similar statistical trends would have been observed for conditions with nearly identical δ^+ (e.g., conditions N1 and P2) using the inner-variable scaling. Therefore, these experimental results clearly demonstrate the critical role Wi plays in polymer-modified TBL, which must be considered if seeking a universal scaling parameter for polymeric flows.

V. SUMMARY AND CONCLUSIONS

The current study experimentally examined velocity profiles on a smooth-walled polymer-modified developing TBL with known and *uniform* polymer properties. Accounting for the shear-induced polymer degradation, friction Reynolds numbers (δ^+) were achieved such that $470 < \delta^+ < 760$, with drag reduction (DR) in the range $15\% < \mathrm{DR} < 44\%$ and Weissenberg number (Wi) ranging from 0.2 to 13. These polymeric conditions were selected to create two specific comparisons to evaluate the role of Wi: (i) conditions P1 and P2 have identical DR (15%) with significantly different Wi (0.2 versus 9), and (ii) conditions P2 and P3 having similar Wi values ($\sim$10) with significantly different DR (15% versus 44%). This is in addition to the Newtonian conditions (N1 and N2), which are used as a baseline case (0% DR) for comparison with the polymeric cases to elucidate the role polymer additives play in DR. The Newtonian cases were compared with established literature [49], with both the mean and fluctuating velocity profiles being in good agreement with the literature [see Figs. 2(a), 3(a), and 4(a)]. These Newtonian conditions provided guidance on the influence of δ^+ on the profiles. This was required since the polymeric conditions were not able to perfectly match the Reynolds number when controlling Wi.

The mean streamwise polymeric velocity profiles revealed the following aspects, showcasing the loss of the well-established universal features of Newtonian profiles: (i) the shrinking of the log-layer with DR, (ii) the intercept constant increasing with DR for LDR, and (iii) κ decreasing for HDR. While DR primarily controlled the shift in the polymeric mean profiles, there was evidence that Wi had a secondary impact consistent with previous findings [26,27]. The inner-variable scaled streamwise fluctuating velocity profiles increased significantly relative to the Newtonian conditions. However, inspection showed that the increase was primarily associated with the decrease in wall friction velocity (u_τ) used to scale the results. If Wi was matched, there was minimal variation in nonscaled velocity fluctuations, and the streamwise fluctuations showed a marginal increase in magnitude with increasing Wi. Conversely, the wall-normal fluctuations were significantly subdued, with the suppression appearing as a function of Wi. Specifically, the DR-matched profiles were significantly different, while the Wi-matched were in close agreement. These observations suggest that the degree of anisotropy in the fluctuating velocity profiles is also a function of Wi. The Reynolds stress profiles had a suppression that was similar to the wall-normal component although not as severe, but still primarily set based on Wi.

The impact of the polymers on coherent structures and the motions they induce (ejection and sweep events) were also investigated. The Wi dependence was explored primarily by comparing conditions N1, P1, and P2, which had similar δ^+ but significantly different Wi. The sweep motions were suppressed throughout the TBL with the suppression proportional to the Wi. The ejections were more complex, but they were suppressed in proportion to Wi for $100 \leqslant y^+ \leqslant 300$. Comparison of the Wi-matched conditions (P2 and P3) showed that inner-variable scaling accounts for the

difference in DR, with δ^+ impacting the outer region in a manner similar to the Newtonian conditions.

Given the evidence that Wi is a critical parameter governing the suppression observed within the fluctuating velocity field, POD analysis was performed to further investigate the modified coherent structures. The reduced number of modes required to recover a given TKE level quantified the reduction in complexity with polymers. Specifically, the percentage of the total energy in the first mode for high Wi polymeric conditions was between 50% and 60%. This is much higher than the 30%–32% observed for the Newtonian cases. Of note, the lowest Wi polymeric condition (P1) (i.e., Wi = 0.2) had only a marginally larger amount of energy contained in the first mode (34%). Thus, the Newtonian conditions (N1 and N2) as well as the polymeric condition with a Wi below unity had almost the same percentage of energy within the first mode in spite of the large range of δ^+ (590–1300). This indicates that the reduction in complexity appears strongly correlated with Wi, even more so than DR. The POD modes also showed that the polymeric conditions elongate the structures in the streamwise direction relative to those in Newtonian flows, indicating the anisotropic structure of the flow field.

The unique set of conditions obtained herein also allow for an overarching observation that the polymeric flow statistics exhibit a parametric dependence on Wi, especially the fluctuating components. This underpins the notion that the "time-criterion" principle [45] due to polymer chains introduces additional flow physics, which is key to the problem of universal scaling in PDR. The results presented herein suggest that polymers chains are effectively removing the energy content at specific scales (i.e., smaller scales) so that there is no longer a mere passing of energy through those scales. This results in an overall abridged wave-number band for the energy cascade, which is consistent with the current interpretation of δ^+, when thought in terms of DR.

ACKNOWLEDGMENT

This work was sponsored in part by the National Science Foundation (NSF) under Grant No. 1604978 (Ronald Joslin, Program Manager).

[1] R. H. J. Sellin, J. W. Hoyt, J. Poliert, and O. Scrivener, The effect of drag reducing additives on fluid flows and their industrial applications, Part 2: Present applications and future proposals, J. Hydraul. Res. **20**, 235 (1982).

[2] G.-C. Liaw, J. L. Zakin, and G. K. Patterson, Effects of molecular characteristics of polymers on drag reduction, AIChE J. **17**, 391 (1971).

[3] P. S. Virk, Drag reduction fundamentals, AIChE J. **21**, 625 (1975).

[4] Y. Dubief, C. M. White, V. E. Terrapon, E. S. Shaqfeh, P. Moin, and S. K. Lele, On the coherent drag-reducing and turbulence-enhancing behaviour of polymers in wall flows, J. Fluid Mech. **514**, 271 (2004).

[5] C. M. White and M. G. Mungal, Mechanics and prediction of turbulent drag reduction with polymer additives, Annu. Rev. Fluid Mech. **40**, 235 (2008).

[6] Z. Saeed and B. R. Elbing, Polymer drag reduction: A review through the lens of coherent structures in wall-bounded turbulent flows, Phys. Fluids **35**, 081304 (2023).

[7] M. Poreh and K. S. Hsu, Diffusion of drag reducing polymers in a turbulent boundary layer, J. Hydronautics **6**, 27 (1972).

[8] D. H. Fruman and M. P. Tulin, Diffusion of a tangential drag-reducing polymer injection on a flat plate at high Reynolds number, J. Ship Res. **20**, 171 (1976).

[9] A. V. Vdovin and A. V. Smol'yakov, Diffusion of polymer solutions in a turbulent boundary layer, J. Appl. Mech. Tech. Phys. **19**, 196 (1978).

[10] A. A. Fontaine, H. L. Petrie, and T. A. Brungart, Velocity profile statistics in a turbulent boundary layer with slot-injected polymer, J. Fluid Mech. **238**, 435 (1992).

[11] H. L. Petrie, S. Deutsch, T. A. Brungart, and A. A. Fontaine, Polymer drag reduction with surface roughness in flat-plate turbulent boundary layer flow, Exp. Fluids **35**, 8 (2003).
[12] E. S. Winkel, G. Oweis, S. Vanapalli, D. R. Dowling, M. Perlin, M. Solomon, and S. Ceccio, High-Reynolds-number turbulent boundary layer friction drag reduction from wall-injected polymer solutions, J. Fluid Mech. **621**, 259 (2009).
[13] B. R. Elbing, D. R. Dowling, M. Perlin, and S. L. Ceccio, Diffusion of drag-reducing polymer solutions within a rough-walled turbulent boundary layer, Phys. Fluids **22**, 045102 (2010).
[14] B. R. Elbing, M. J. Solomon, M. Perlin, D. R. Dowling, and S. L. Ceccio, Flow-induced degradation of drag-reducing polymer solutions within a high-Reynolds-number turbulent boundary layer, J. Fluid Mech. **670**, 337 (2011).
[15] P. S. Virk, H. S. Mickley, and K. A. Smith, The ultimate asymptote and mean flow structure in Toms' phenomenon, J. Appl. Mech. Mech. **37**, 488 (1970).
[16] M. Warholic, H. Massah, and T. Hanratty, Influence of drag-reducing polymers on turbulence: Effects of Reynolds number, concentration and mixing, Exp. Fluids **27**, 461 (1999).
[17] B. R. Elbing, E. S. Winkel, S. L. Ceccio, M. Perlin, and D. R. Dowling, High-Reynolds-number turbulent-boundary-layer wall-pressure fluctuations with dilute polymer solutions, Phys. Fluids **22**, 085104 (2010).
[18] B. Elbing, M. Perlin, D. Dowling, and S. Ceccio, Modification of the mean near-wall velocity profile of a high-Reynolds number turbulent boundary layer with the injection of drag-reducing polymer solutions, Phys. Fluids **25**, 085103 (2013).
[19] J. E. Koskie and W. G. Tiederman, Polymer drag reduction of a zero-pressure-gradient boundary layer, Phys. Fluids **3**, 2471 (1991).
[20] T. Wei and W. Willmarth, Modifying turbulent structure with drag-reducing polymer additives in turbulent channel flows, J. Fluid Mech. **245**, 619 (1992).
[21] P. Ptasinski, B. Boersma, F. Nieuwstadt, M. Hulsen, B. Van den Brule, and J. Hunt, Turbulent channel flow near maximum drag reduction: Simulations, experiments and mechanisms, J. Fluid Mech. **490**, 251 (2003).
[22] C. M. White, V. S. R. Somandepalli, and M. G. Mungal, The turbulence structure of drag-reduced boundary layer flow, Exp. Fluids **36**, 62 (2004).
[23] Y. X. Hou, V. S. R. Somandepalli, and M. G. Mungal, Streamwise development of turbulent boundary-layer drag reduction with polymer injection, J. Fluid Mech. **597**, 31 (2008).
[24] M. Escudier, A. Nickson, and R. Poole, Turbulent flow of viscoelastic shear-thinning liquids through a rectangular duct: Quantification of turbulence anisotropy, J. Non-Newtonian Fluid Mech. **160**, 2 (2009).
[25] C. White, Y. Dubief, and J. Klewicki, Re-examining the logarithmic dependence of the mean velocity distribution in polymer drag reduced wall-bounded flow, Phys. Fluids **24**, 021701 (2012).
[26] J. R. Elsnab, J. P. Monty, C. M. White, M. M. Koochesfahani, and J. C. Klewicki, High-fidelity measurements in channel flow with polymer wall injection, J. Fluid Mech. **859**, 851 (2019).
[27] B. Elbing, Impact of polymer degradation on past studies of the mean velocity profile in turbulent boundary layers, J. Fluids Eng. **143**, 081101 (2021).
[28] S. A. Vanapalli, M. T. Islam, and M. J. Solomon, Scission-induced bounds on maximum polymer drag reduction in turbulent flow, Phys. Fluids **17**, 095108 (2005).
[29] Y. Farsiani, Z. Saeed, and B. R. Elbing, Drag reduction performance of mechanically degraded dilute polyethylene oxide solutions, J. Fluids Eng. **142**, 091201 (2020).
[30] B. R. Elbing, L. Daniel, Y. Farsiani, and C. E. Petrin, Design and validation of a recirculating, high-Reynolds number water tunnel, J. Fluids Eng. **140**, 081102 (2018).
[31] M. Acharya, J. Bornstein, and M. Escudier, Turbulent boundary layers on rough surfaces, Exp. Fluids **4**, 33 (1986).
[32] M. P. Schultz, The relationship between frictional resistance and roughness for surfaces smoothed by sanding, J. Fluids Eng. **124**, 492 (2002).
[33] B. Wieneke, Piv uncertainty quantification from correlation statistics, Meas. Sci. Technol. **26**, 074002 (2015).
[34] A. Sciacchitano and B. Wieneke, PIV uncertainty propagation, Meas. Sci. Technol. **27**, 084006 (2016).

[35] A. A. Draad, G. Kuiken, and F. Nieuwstadt, Laminar–turbulent transition in pipe flow for Newtonian and non-Newtonian fluids, J. Fluid Mech. **377**, 267 (1998).
[36] M. Lander, Preparation and characterization of polyethylene-oxide (PEO) solution, M.S. thesis, Oklahoma State University, Stillwater, 2018.
[37] B. McKeon, Measurement of pressure with wall tappings, in *Handbook of Experimental Fluid Mechanics*, edited by C. Tropea, A. L. Yarin, and J. F. Foss (Springer, Berlin, Heidelberg, 2007), pp. 180–184.
[38] P. S. Virk, E. Merrill, H. Mickley, K. Smith, and E. Mollo-Christensen, The Toms phenomenon: Turbulent pipe flow of dilute polymer solutions, J. Fluid Mech. **30**, 305 (1967).
[39] P. Virk, Drag reduction in rough pipes, J. Fluid Mech. **45**, 225 (1971).
[40] H. J. Choi and M. S. Jhon, Polymer-induced turbulent drag reduction, Ind. Eng. Chem. Res. **35**, 2993 (1996).
[41] B. E. Owolabi, D. J. Dennis, and R. J. Poole, Turbulent drag reduction by polymer additives in parallel-shear flows, J. Fluid Mech. **827**, R4 (2017).
[42] F. Bailey Jr. and R. Callard, Some properties of poly (ethylene oxide)[1] in aqueous solution, J. Appl. Polym. Sci. **1**, 56 (1959).
[43] B. H. Zimm, Dynamics of polymer molecules in dilute solution: Viscoelasticity, flow birefringence and dielectric loss, J. Chem. Phys. **24**, 269 (1956).
[44] V. N. Kalashnikov, Shear-rate dependent viscosity of dilute polymer solutions, J. Rheology **38**, 1385 (1994).
[45] J. L. Lumley, The structure of inhomogeneous turbulent flows, in *Atmospheric Turbulence and Radio Wave Propagation*, edited by A. M. Yaglom and V. I. Tartarsky (Nauka, Moscow, 1967), pp. 166–177.
[46] G. Berkooz, P. Holmes, and J. L. Lumley, The proper orthogonal decomposition in the analysis of turbulent flows, Annu. Rev. Fluid Mech. **25**, 539 (1993).
[47] S. B. Pope, *Turbulent Flows* (Cambridge University Press, New York, NY, 2000).
[48] Y. Wu, A study of energetic large-scale structures in turbulent boundary layer, Phys. Fluids **26**, 045113 (2014).
[49] D. B. De Graaff and J. K. Eaton, Reynolds-number scaling of the flat-plate turbulent boundary layer, J. Fluid Mech. **422**, 319 (2000).
[50] H. M. Nagib and K. A. Chauhan, Variations of von Karman coefficient in canonical flows, Phys. Fluids **20**, 101518 (2008).
[51] G. F. Oweis, E. S. Winkel, J. M. Cutbrith, S. L. Ceccio, M. Perlin, and D. R. Dowling, The mean velocity profile of a smooth-flat-plate turbulent boundary layer at high Reynolds number, J. Fluid Mech. **665**, 357 (2010).
[52] M. Warholic, D. Heist, M. Katcher, and T. Hanratty, A study with particle-image velocimetry of the influence of drag-reducing polymers on the structure of turbulence, Exp. Fluids **31**, 474 (2001).
[53] A. Townsend, *The Structure of Turbulent Shear Flow* (Cambridge University Press, New York, NY, 1976).
[54] I. Marusic, R. Mathis, and N. Hutchins, Predictive model for wall-bounded turbulent flow, Science **329**, 193 (2010).
[55] J. M. Wallace, Quadrant analysis in turbulence research: History and evolution, Annu. Rev. Fluid Mech. **48**, 131 (2016).
[56] Y. Farsiani, Z. Saeed, B. Jayaraman, and B. R. Elbing, Modification of turbulent boundary layer coherent structures with drag reducing polymer solution, Phys. Fluids **32**, 015107 (2020).
[57] K. Kim, C.-F. Li, R. Sureshkumar, S. Balachandar, and R. J. Adrian, Effects of polymer stresses on eddy structures in drag-reduced turbulent channel flow, J. Fluid Mech. **584**, 281 (2007).
[58] G. Offen and S. Kline, A proposed model of the bursting process in turbulent boundary layers, J. Fluid Mech. **70**, 209 (1975).
[59] C. R. Smith, J. Walker, A. Haidari, and U. Sobrun, On the dynamics of near-wall turbulence, Philos. Trans. R. Soc. London Ser. A **336**, 131 (1991).
[60] S. J. Kline, W. C. Reynolds, F. Schraub, and P. Runstadler, The structure of turbulent boundary layers, J. Fluid Mech. **30**, 741 (1967).
[61] H. Kim, S. Kline, and W. Reynolds, The production of turbulence near a smooth wall in a turbulent boundary layer, J. Fluid Mech. **50**, 133 (1971).

[62] S. K. Robinson, Coherent motions in the turbulent boundary layer, Annu. Rev. Fluid Mech. **23**, 601 (1991).
[63] J. Sheng, E. Malkiel, and J. Katz, Buffer layer structures associated with extreme wall stress events in a smooth wall turbulent boundary layer, J. Fluid Mech. **633**, 17 (2009).
[64] M. Metzger, A. Fershtut, C. Kunkel, and J. Klewicki, Reynolds number scaling of pocket events in the viscous sublayer, Phys. Rev. Fluids **2**, 124602 (2017).
[65] J. Jiménez and A. Pinelli, The autonomous cycle of near-wall turbulence, J. Fluid Mech. **389**, 335 (1999).
[66] W. G. Tiederman, T. S. Luchik, and D. Bogard, Wall-layer structure and drag reduction, J. Fluid Mech. **156**, 419 (1985).
[67] R. J. Adrian, Hairpin vortex organization in wall turbulence, Phys. Fluids **19**, 041301 (2007).
[68] J. Zhou, R. J. Adrian, S. Balachandar, and T. Kendall, Mechanisms for generating coherent packets of hairpin vortices in channel flow, J. Fluid Mech. **387**, 353 (1999).
[69] Y. Shah, S. Ghaemi, and S. Yarusevych, Experimental investigation of extreme skin friction events in polymer drag-reduced turbulent boundary layers, Exp. Fluids **63**, 27 (2022).
[70] M. Tabor and P. De Gennes, A cascade theory of drag reduction, Europhys. Lett. **2**, 519 (1986).